RSC Advances

PAPER

View Article Online
View Journal | View Issue



Cite this: *RSC Adv.*, 2018, **8**, 15853

# Enhanced visible-light photocatalytic activity and photostability of $Ag_3PO_4/Bi_2WO_6$ heterostructures toward organic pollutant degradation and plasmonic Z-scheme mechanism†

Fengyan Ma,[a] Qilin Yang,[a] Zhengjun Wang,[a] Yahong Liu,[a] Jianjiao Xin,[a] Jingjing Zhang,[a] Yuting Hao[a] and Li Li *[ab]

Novel $Ag_3PO_4/Bi_2WO_6$ heterostructured materials with enhanced visible-light catalytic performance were successfully synthesized by assembly combined with a hydrothermal treatment. The microstructures, morphologies, and optical properties of the prepared samples were characterized by multiple techniques. The irregular $Ag_3PO_4$ nanospheres dispersed on the surface of $Bi_2WO_6$ nanoflakes, and their catalytic performances were evaluated *via* the degradation of organic pollutants including rhodamine B (RB), methylene blue (MB), crystal violet (CV), methyl orange (MO), and phenol (Phen) under visible-light irradiation. The resulting $Ag_3PO_4/Bi_2WO_6$ heterostructured materials displayed higher photocatalytic activity than that of either pure $Bi_2WO_6$ or $Ag_3PO_4$. The enhanced photocatalytic activity was due to the good formation of heterostructures, which could not only broaden the spectral response range to visible light but also effectively promoted the charge separation. Meanwhile, the reasonable photoreactive plasmonic Z-scheme mechanism was carefully investigated on the basic of the reactive species scavenging tests, photoelectrochemical experiments, and photoluminescence (PL) spectrum. In addition, the excellent photostability of $Ag_3PO_4/Bi_2WO_6$ was obtained, which Ag formed at the early photocatalytic reaction acted as the charge transmission-bridge to restrain the further photoreduction of $Ag_3PO_4$.

Received 16th February 2018
Accepted 21st April 2018

DOI: 10.1039/c8ra01477a

rsc.li/rsc-advances



## 1. Instruction

Recently, semiconductor photocatalysis has attracted more and more attention as a green, highly efficient technology for resolving the current energy and environmental problems.[1–3] Photocatalysts based on $TiO_2$, ZnO are inactive under visible light irradiation due to their wide bandgap energy and improper band position, which requires ultraviolet irradiation that only accounts for less than 5% of the solar energy.[4–6] And the main reason for their poor photocatalytic activity might be due to the strong recombination of photogenerated electron–hole ($e^-$–$h^+$) pairs, which is a widespread phenomenon among semiconductor photocatalysts. Therefore, it is still challenging to extend the photo-response range and improve the charge separation efficiency of the semiconductor photocatalysts for satisfying the requirements of applications.

Recently, Bi-based semiconductor materials, such as $Bi_2WO_6$, $BiVO_4$, $Bi_2MO_6$, $Bi_2Mo_2O_9$, $Bi_{24}O_{31}Br_{10}$, and BiOBr, have attracted widespread attention in photocatalytic application owing to the relatively narrow gap, nontoxicity, chemical inertness, stability, and sunlight utilization for wastewater treatment.[7–14] Among the Bi-based semiconductor materials, $Bi_2WO_6$, as a typical aurivillius oxide, is regarded one of the ideal photocatalyst materials because of its unique layered structure feature and relatively high visible photocatalytic activity. However, the photocatalytic activity of bare $Bi_2WO_6$ is limited by the high recombination rate of photogenerated $e^-$–$h^+$ pairs and the low absorption capacity of visible-light (less than 450 nm).[15,16] Therefore, how to improve separation efficiency of photoinduced $e^-$–$h^+$ pairs during the photocatalytic reactions becomes a key issue for developing the $Bi_2WO_6$-based photocatalysts.

More recently, among the reported Ag-based semiconductors, especially silver orthophosphate ($Ag_3PO_4$), which has a strong absorption ($\lambda$ < 530 nm), has been considered as a promising photocatalyst with outstanding visible-light catalytic activity.[17,18] Meanwhile, $Ag_3PO_4$ possesses extremely oxidation power, which not only oxidizes $H_2O$ to produce $O_2$ but also degrades organic pollutants under visible-light

[a]*College of Chemistry and Chemical Engineering, Qiqihar University, Qiqihar 161006, Heilongjiang, P. R. China*

[b]*College of Materials Science and Engineering, Qiqihar University, Qiqihar 161006, Heilongjiang, P. R. China. E-mail: qqhrlili@126.com*

† Electronic supplementary information (ESI) available. DOI: 10.1039/c8ra01477a

irradiation.[19–22] However, there are some flaws limit its extensive use as following: (1) $Ag_3PO_4$ is slightly soluble in water due to its larger solubility product constant ($K_{sp} = 1.6 \times 10^{-16}$)[23]; (2) as the photosensitive material, it can be easily corroded by light and reduced to $Ag^0$ in the photocatalytic process without electron acceptors;[24] (3) it suffers from the fast recombination of photogenerated charge-carries.[25]

In the present study, $Ag_3PO_4$ is introduced on the basis of the following points: (1) $Ag_3PO_4$ is a narrow-semiconductor ($E_g$ = 2.4 eV), and its introduction is beneficial to extend the light response of $Bi_2WO_6$ to a higher wavelength region and thereby decreasing its band gap; (2) two semiconductors possess the matching band structure, similar band gap, and the proper molar ratio, and build effective heterostructures, which promote the efficient separation of the $e^-$–$h^+$ pairs and therefore increasing the quantum yield; (3) part $Ag_3PO_4$ is reduced to metallic Ag during the initial photocatalytic reaction. It is precisely this part of the elemental silver can be used as a solid-state electron mediator to accelerate charge separation through Z-scheme system, which improve the charge separation, prevent the continuing reductive decomposition of $Ag_3PO_4$, and enhance its stability. Hence, the coupling of $Bi_2WO_6$ with $Ag_3PO_4$ to form heterostructures is considered to be one of the most promising methods to improve the visible-light-driven catalytic performance of photocatalysts ($Bi_2WO_6$ or $Ag_3PO_4$) because the heterostructures not only broaden the spectral response range to visible light but also promote the charge separation. This point is confirmed by the deposition of $Ag_3PO_4$ onto certain semiconductor materials. Please see the Table 1 (ESI†). Table 1 summarizes the detailed information on literature reported $Ag_3PO_4$ photocatalysts. Compared with the semiconductor materials, such as ZnO,[26] graphene[27] (G), $InVO_4$/$BiVO_4$,[28] and $Bi_2MoO_6$,[29] $Bi_2WO_6$ as support can well improve the photocatalytic activity of $Ag_3PO_4$.

Among a good deal of the heterojunction photocatalysts, the all-solid-state Z-scheme photocatalytic system possesses advantages over improving separation ratio of photo-induced $e^-$–$h^+$ pairs and enhancing the stability of photocatalyst. In general, the all-solid-state Z-scheme photocatalytic system consists of two different semiconductor materials and an electron mediator. Notably, metallic Ag as a solid-state electron mediator would contribute to the construction of Z-scheme system. Recently, Yuan *et al.* successfully prepared $Ag_3PO_4$/$CuBi_2O_4$ photocatalyst and formed $Ag_3PO_4$/Ag/$CuBi_2O_4$ photocatalyst during the photocatalytic degradation process, which can enhance photocatalytic activity and stability of photocatalyst through the formation of Z-scheme system.[30] Liu *et al.* also designed a novel visible-light-driven Ag/$Ag_3PO_4$/$WO_3$ Z-scheme heterostructures by a facile deposition–precipitation method followed by photoreducing $Ag^+$ into metallic Ag. The Ag/$Ag_3PO_4$/$WO_3$ showed enhanced photocatalytic RhB efficiency, indicating the formed Z-scheme heterostructures could efficiently promote the separation and transfer of photogenerated $e^-$–$h^+$ pairs.[31] So the combination of $Bi_2WO_6$ and $Ag_3PO_4$ to construct Z-scheme would be an efficient strategy.

Table 1 Textural parameters of various materials

| Samples | $S_{BET}$ ($m^2\ g^{-1}$) | $V_p$ ($cm^3\ g^{-1}$) | $D_p$ (nm) |
|---|---|---|---|
| $Ag_3PO_4$ | 8.06 | 0.038 | 11.47 |
| $Ag_3PO_4/Bi_2WO_6$-0.3 | 14.50 | 0.049 | 9.46 |
| $Ag_3PO_4/Bi_2WO_6$-0.5 | 18.21 | 0.070 | 10.74 |
| $Bi_2WO_6$ | 43.55 | 0.16 | 10.44 |

To the best of our knowledge, there is less report on the achievement of $Bi_2WO_6$-based heterojunction by the introduction of $Ag_3PO_4$. For instance, Somchai Thongtem prepared $Ag_3PO_4/Bi_2WO_6$ toward RB (5 ppm) degradation efficiency can reach 100% after 80 min visible-light illumination.[32] Because it is still not sufficient for practical application. It is necessary to further improve the photocatalytic activity of $Ag_3PO_4/Bi_2WO_6$. In addition, there is no corresponding research reports to discuss the $Ag_3PO_4/Bi_2WO_6$ for pollutants' removal based on the plasmonic Z-scheme mechanism. Therefore, it is meaningful to apply the SPR effect of Ag nanoparticles into the hybrid composite to design highly efficient visible-light-driven photocatalysts based on Z-scheme charge transfer mechanism.

Herein, we successfully fabricated $Ag_3PO_4/Bi_2WO_6$ heterostructures *via* the assembly combined with a hydrothermal technique. The $Ag_3PO_4/Bi_2WO_6$ heterostructures displayed enhanced photocatalytic performance toward organic pollutants (including rhodamine B (RB), phenol (Phen), methyl orange (MO), crystal violet (CV), and methylene blue (MB)) degradation under visible-light irradiation. Subsequently, microstructures, surface chemical states, specific surface areas, optical, and photoelectrochemical properties of $Ag_3PO_4/Bi_2WO_6$ heterojunction were systematically studied. Meanwhile, a possible visible-light-induced photocatalytic mechanism of $Ag_3PO_4/Bi_2WO_6$ heterostructures was proposed.

## 2. Experiment section

### 2.1 Preparation of photocatalysts

**2.1.1 Preparation of $Bi_2WO_6$.** All the reagents used in the experiment were of analytic grades, commercially purchased and used without further purification. In a typical process, 0.972 g $Bi(NO_3)_3$ and 0.329 g $Na_2WO_4$ were dissolved in glacial acetic acid (10 mL) and $H_2O$ (10 mL), respectively. Then the $Na_2WO_4$ solution was dropwise added into $Bi(NO_3)_3$ solution. After being continuously stirred for 4 h, the mixture was transferred to Teflon-coated autoclave and held at 150 °C for 20 h followed by cooling at room temperature naturally. To remove any residue of by-products and reactants, the obtained $Bi_2WO_6$ was washed with deionized water several times and dried at 80 °C for 24 h.

**2.1.2 Preparation of $Ag_3PO_4/Bi_2WO_6$.** $Ag_3PO_4/Bi_2WO_6$ composites with the different molar ratio were synthesized as follows. 1.092 g $AgNO_3$ and 0.762 g $Na_3PO_4$ were dissolved in deionized water (10 mL) and stirred for 30 min, respectively. Then $Na_3PO_4$ solution was dropwise added into the $AgNO_3$ solution to form yellow sediments with stirring for 2 h. Subsequently, a certain amount of as-prepared $Bi_2WO_6$ was slowly added to the above mixture and stirred for 4 h followed by drying at 60 °C for 24 h. Ultimately, the obtained $Ag_3PO_4/Bi_2WO_6$ samples were collected by washing, filtration, and

 

drying at 60 °C for 48 h. The series of photocatalysts prepared were labeled as $Ag_3PO_4/Bi_2WO_6$-*x*, where *x* presents the molar ratio of $Bi_2WO_6$ to $Ag_3PO_4$. Pure $Ag_3PO_4$ was acquired in the absence of $Bi_2WO_6$ through the same process.

### 2.2 Characterization of photocatalysts

The crystal structures were obtained on a Bruker-AXS (D8) X-ray diffractometer with Cu Kα radiation. X-ray photoelectron spectroscopy (XPS) characterization was carried out on an ESCALAB 250Xi spectrometer equipped with Al Kα radiation at 300 W. $N_2$ adsorption–desorption isotherm analysis of samples were obtained at 77 K using Micromeritics 3H-2000PS2. The morphologies of synthesized samples were analyzed using a scanning electron microscope (SEM) (Hitachi S-4300) and transmission electron microscope (TEM) and high resolution transmission electron microscope (HRTEM) (JEM-2100F). The UV-visible diffuse reflectance spectra (UV-vis-DRS) were recorded using a UV-vis spectrophotometer (TU-1901) over the wavelength range of 200–800 nm using $BaSO_4$ as the reflectance standard material. Fourier transform infrared (FT-IR) spectra were recorded using an FT-IR spectrophotometer (PE Company, America). Photoluminescence spectra (PL) were obtained by a Hitachi F-7000 spectrofluorometer with an excitation wavelength of 360 nm, and all the samples were pressed into pellets in the sample holder.

### 2.3 Photocatalytic tests

Photocatalytic activities of the $Ag_3PO_4/Bi_2WO_6$ heterostructures were studied by monitoring the degradation behaviors of organic contaminants, including RB, Phen, MO, CV, and MB. The photocatalytic experiments were carried out in a hollow cylindrical photoreactor equipped with a water jacket. 400 W Xe lamp ($\lambda > 410.0$ nm; moreover, the inner sleeve was made of No. 11 glasses to filter out ultraviolet from the Xe lamp) was used as the visible-light source. The Xe lamp was positioned within the inner part of the photoreactor and cooling water was circulated through a pyrex jacket surrounding the lamp to keep room temperature. In a typical experimental procedure, 200 mg of catalyst was placed into 220 mL of dye (50 ppm) or Phen (25 ppm) solution *via* ultrasonication for 10 min, and magnetically stirred in the dark for 1 h to establish the adsorption–desorption equilibrium between the catalyst and organic contaminant. Then the suspension was exposed to visible light irradiation under magnetic stirring. 4 mL of the suspension was collected at a regular time interval and analyzed after centrifugation. The dye concentration was analyzed by UV-vis spectrophotometer (TU-1901) at the maximum absorption spectra. Changes of Phen concentrations were monitored by a Yilite P230II HPLC: $C_{18}$ column, UV detector ($\lambda = 270$ nm), methanol/water (50/50, v/v), and 1 mL $min^{-1}$.

### 2.4 Photoelectrochemical experiments

Electrochemical measurements were carried out in a traditional three-electrode system (CHI660E, China). Indium-tin oxide (ITO) glass electrode (1 $cm^2$), saturated calomel electrode (SCE), and Pt sheet were used as the working electrode, reference electrode, and the counter electrode, respectively. The sample mixed with Nafion ionomer was dissolved ethanol aqueous solution to obtain 5 mg $L^{-1}$ suspension. And then the suspension was uniformly drop-coated onto the clean ITO electrode surface and dried in air. A Xe lamp was used as the light source, and aqueous $Na_2SO_4$ solution (0.01 mol $L^{-1}$) served as the electrolyte. All the experiments were performed at room temperature (about 25 °C). The photocurrent was measured under light illumination from a 400 W Xe lamp. The electrochemical impedance study was carried out over a frequency domain of 1 Hz to 100 kHz with a sinusoidal perturbation potential of 5 mV.

## 3. Results and discussion

### 3.1 Characteristics of microstructures of $Ag_3PO_4/Bi_2WO_6$

XRD is used to investigate the crystal structure of the samples. As displayed in Fig. 1, the distinct diffraction peaks of $Bi_2WO_6$ can be found 28.3°, 32.8°/32.9°, 47.1°, 56.0°, 58.5°, 68.8°, 75.9°, and 78.5°, which can be attributed to the (131), (200)/(002), (202), (133), (262), (400), (193), and (204) crystal planes of orthorhombic phase of $Bi_2WO_6$ (JCPDS 39-0256). While for pure $Ag_3PO_4$, the characteristic peaks of 21.7° (110), 29.7° (200), 33.3° (210), 36.5° (211), 47.8° (310), 52.6°(222), 54.9°(320), 57.2° (321), 61.8°(400), and 71.8°(421) are well indexed as the body-centered cubic phase of $Ag_3PO_4$ (JCPDS 06-0505). In case of $Ag_3PO_4/Bi_2WO_6$ composites, they show the coexistence of $Bi_2WO_6$ phase and $Ag_3PO_4$ phase. Furthermore, the peak intensity of $Bi_2WO_6$ increases with increasing the $Bi_2WO_6$ loading, while the peak intensity of $Ag_3PO_4$ lowers simultaneously. However, the peak position of $Ag_3PO_4$ does not significantly change, which indicates $Bi_2WO_6$ is not incorporated into $Ag_3PO_4$ lattice. In addition, no diffraction peaks of Ag or other impurities are found.

X-ray photoelectron spectroscopy (XPS) as surface analytic technique is employed to detect the electronic structures of $Ag_3PO_4$, $Bi_2WO_6$, and $Ag_3PO_4/Bi_2WO_6$ composites. Fig. 2a shows the high-resolution XPS spectra of Ag of the $Ag_3PO_4$ and $Ag_3PO_4/Bi_2WO_6$ composite catalysts. The typical peaks of Ag 3d at 368.0 eV (Ag $3d_{5/2}$) and 374.0 eV (Ag $3d_{3/2}$) are ascribed to $Ag^+$ in $Ag_3PO_4$.[33] After the $Bi_2WO_6$ introduction, the binding energy of spin-obit Ag 3d is divided into two peaks at 368.3 and 374.3 eV (ref. 24 and 34), which is 0.3 eV higher than those of $Ag_3PO_4$.

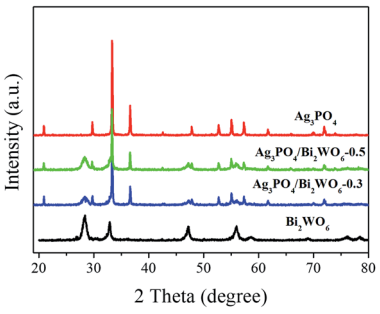


Fig. 1 XRD patterns of the pristine $Bi_2WO_6$, $Ag_3PO_4$, and $Ag_3PO_4/Bi_2WO_6$ composites.

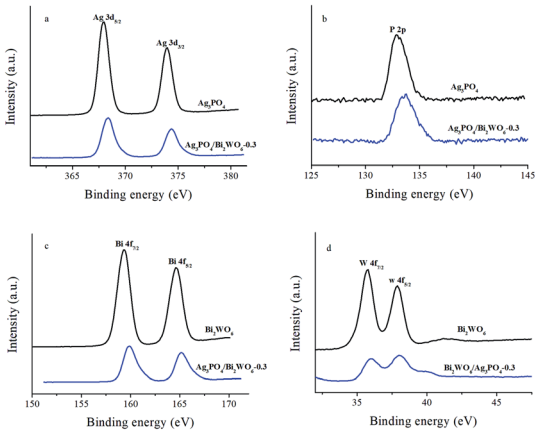


Fig. 2 The high-resolution XPS spectra of Ag 3d (a), P 2p (b), Bi 4f (c), and W 4f (d) for the $Ag_3PO_4$, $Bi_2WO_6$, and $Ag_3PO_4/Bi_2WO_6$-0.3.

The characteristic peaks of Ag nanocrystals existing on the surface of $Ag_3PO_4$ and $Ag_3PO_4/Bi_2WO_6$ are not found, suggesting no $Ag^0$ was formed during the preparation of the catalysts. Compared with pure $Ag_3PO_4$, the binding energy of P 2p of $Ag_3PO_4/Bi_2WO_6$ is turned from 132.8 eV to a higher value of 133.8 eV (Fig. 2b). As shown in Fig. 2c, the peaks located at 159.3 eV, 164.6 eV, and 159.9 eV, 165.2 eV correspond to the Bi $4f_{7/2}$ and Bi $4f_{5/2}$ of $Bi_2WO_6$ and $Ag_3PO_4/Bi_2WO_6$, respectively, implying the bismuth species in the composite is $Bi^{3+}$ cations. The peaks for W $4f_{7/2}$ (35.98 eV) and W $4f_{5/2}$ (37.98 eV) can be attributed to a six-valent oxidation state for $W^{6+}$ in $Ag_3PO_4/Bi_2WO_6$, meaning 0.2 and 0.1 eV deviation of $4f_{7/2}$ and $4f_{5/2}$ relative to the values in pure $Bi_2WO_6$ (Fig. 2d).

The O 1s high-resolution XPS spectra of samples are provided in Fig. S1 (ESI†). The O 1s XPS spectra of $Bi_2WO_6$ ($Ag_3PO_4$) show three individual peaks with the binding energies of 530.2 eV (530.2 eV, denoted as O 1s(1)), 531.6 eV (531.3 eV, denoted as O 1s(2)), and 533.1 eV (533.1 eV, denoted as O 1s(3)), which can be attributed to the lattice oxygen in $Bi_2WO_6$ ($Ag_3PO_4$), the external hydroxyl groups, and adsorbed oxygen species at the surface of the composite.[35–37] For $Ag_3PO_4/Bi_2WO_6$-0.3, the binding energies of O 1s orbits are 529.9 eV, 531.4 eV, and 533.1 eV, respectively. And they also display more or less lower energy shift compared with individual counterparts. The variations of the binding energies of Ag 3d, P 2p, Bi 4f, W 4f, and O 1s are attributed to chemical interactions between $Bi_2WO_6$ and $Ag_3PO_4$, which proves the formation of heterostructures and facilitates interfacial charge transfer, leading to the improved photocatalytic activity of $Ag_3PO_4/Bi_2WO_6$ nanocomposites. Beyond that, the tight chemical interactions can improve the structural stability of photocatalyst. The similar results were also reported by another group.[38,39]

FT-IR spectra were carried out to investigate the presence of $Ag_3PO_4$ and $Bi_2WO_6$ in the $Ag_3PO_4/Bi_2WO_6$ composite. As shown in Fig. 3, the typical peaks located at 577.8 $cm^{-1}$, 731.6 $cm^{-1}$, and 1384 $cm^{-1}$ are attributed to the Bi–O, W–O, and W–O–W bridging stretching modes, respectively, which indicates the existence of $Bi_2WO_6$.[40,41] For pure $Ag_3PO_4$, the stronger peak at

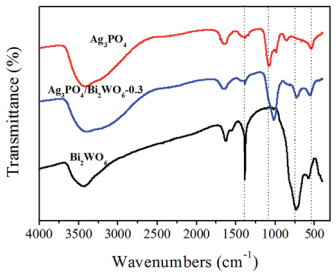


Fig. 3 FTIR spectra of $Bi_2WO_6$, $Ag_3PO_4$, and $Ag_3PO_4/Bi_2WO_6$.

543.1 $cm^{-1}$ is ascribed to bending vibration of O=P–O. The other absorption bands at 859.9 $cm^{-1}$ and 1076.4 $cm^{-1}$ are assigned to the symmetric and asymmetric stretching vibrations of P–O–P rings.[42] After the $Bi_2WO_6$ introduction, the typical peaks corresponding Bi–O, W–O, and W–O–W stretching modes in $Ag_3PO_4/Bi_2WO_6$ composite disappear, shift to lower value, and become weak, respectively. However, compared with pure $Ag_3PO_4$, the wavenumbers of P–O–P symmetric and asymmetric stretching vibrations shift to lower values of 817.6 $cm^{-1}$ and 1017.5 $cm^{-1}$. Meanwhile, that of O=P–O changes from 543.1 $cm^{-1}$ to 559.3 $cm^{-1}$. In addition, the bands at 3400 $cm^{-1}$ and 1654 $cm^{-1}$ are related to the –OH stretching and vibration of adsorbed $H_2O$ on the surface of photocatalysts. These results further verify the interaction between $Bi_2WO_6$ and $Ag_3PO_4$, meaning $Bi_2WO_6$ was successfully modified $Ag_3PO_4$.

The typical morphologies of $Ag_3PO_4$, $Bi_2WO_6$, and $Ag_3PO_4/Bi_2WO_6$ composites were characterized by SEM images. From Fig. 4a, $Ag_3PO_4$ shows irregular spherical morphology with a diameter of 100–180 nm. While $Bi_2WO_6$ exhibits a typical structure of nanoflakes consist of nanoparticles with the side length of 50–250 nm (Fig. 4b). Fig. 4c illustrates the typical SEM image of $Ag_3PO_4/Bi_2WO_6$-0.3, where irregular spherical $Ag_3PO_4$ nanoparticles disperse on the surface of $Bi_2WO_6$ nanoflakes. These tiny particles intertwine with each other, suggesting that $Ag_3PO_4$ nanoparticles can restrain the agglomeration of $Bi_2WO_6$ nanoflakes.

The morphological and microstructural details of $Ag_3PO_4/Bi_2WO_6$-0.3 are obtained by TEM and HRTEM technique. As

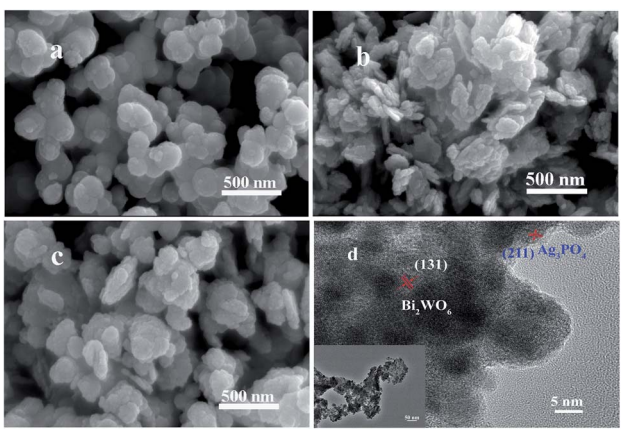


Fig. 4 SEM images of $Ag_3PO_4$ (a), $Bi_2WO_6$ (b), $Ag_3PO_4/Bi_2WO_6$-0.3 (c), and HRTEM (d) and TEM images (inset d) of $Ag_3PO_4/Bi_2WO_6$-0.3.

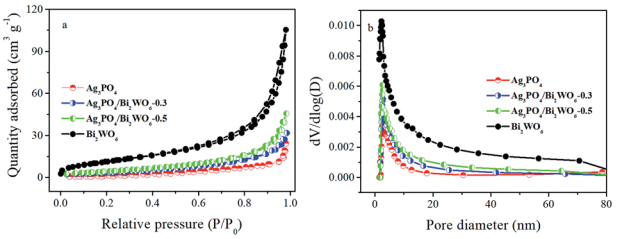


Fig. 5 $N_2$ adsorption–desorption isotherm curves (a) and pore size distribution (b) of the as-prepared samples.

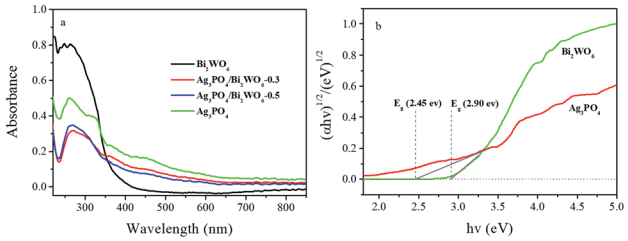


Fig. 6 UV-vis DRS (a) and the plots of $(\alpha h\nu)^{1/2}$ *versus* photon energy for the band gap energies (b) of $Ag_3PO_4$, $Bi_2WO_6$, and $Ag_3PO_4/Bi_2WO_6$ photocatalysts.

displayed in the inset of Fig. 4d, the $Ag_3PO_4$ irregular spheres disperse over the surface of $Bi_2WO_6$ nanoflakes, which is coincided with the aforementioned SEM observations. From the HRTEM image of $Ag_3PO_4/Bi_2WO_6$-0.3 (Fig. 4d), the lattice distances for the $Bi_2WO_6$ (131) and $Ag_3PO_4$ (211) facets are measured to be 0.315 and 0.245 nm, respectively, which is in well accordance with the XRD results. Furthermore, to further prove the formation of heterostructure, the energy dispersive spectroscopy (EDS) elemental mapping of $Ag_3PO_4/Bi_2WO_6$-0.3 was performed. As shown in Fig. S2(b–f) (ESI†), $Ag_3PO_4$ and $Bi_2WO_6$ are relatively uniform dispersion and well connected, which is in accordance with that of SEM and TEM images. Therefore, according to the above results, it gives solid evidence for the formation of heterostructure between $Bi_2WO_6$ and $Ag_3PO_4$.

The BET specific surface area and the porous structure of the samples were analyzed by nitrogen adsorption–desorption isotherms, the results shown in Table 1. As shown in Fig. 5a, the $N_2$ isotherms of samples show characteristic type IV isotherms with H3 hysteresis loops, implying the presence of mesopores in the size of 2–50 nm. This result can be further proved by the pore size distribution analysis (Fig. 5b). And the specific surface area of pure $Ag_3PO_4$, $Ag_3PO_4/Bi_2WO_6$-0.3, $Ag_3PO_4/Bi_2WO_6$-0.5, and $Bi_2WO_6$ is 8.06, 14.50, 18.21, and 43.55 $m^2\ g^{-1}$, respectively. The BJH absorption cumulative pore volume increases from 0.038 to 0.070 $cm^3\ g^{-1}$ after incorporation with $Bi_2WO_6$. The results imply the specific surface area and pore volume of $Ag_3PO_4/Bi_2WO_6$ slight enhance with increasing $Bi_2WO_6$ loading contrast with $Ag_3PO_4$. But the specific surface area and pore volume have no obvious change among these samples, which play a minor role in the enhanced photocatalytic activity of $Ag_3PO_4/Bi_2WO_6$ composite.

### 3.2 Optical absorption properties

The optical absorbance properties and gap energies of the $Ag_3PO_4$, $Bi_2WO_6$, and $Ag_3PO_4/Bi_2WO_6$ composites were determined using the UV-vis-DRS, and the results were displayed in Fig. 6. From Fig. 6a, the pure $Bi_2WO_6$ exhibits strong absorbance in the wavelengths shorter than 450 nm owing to the intrinsic band-gap transition,[43] and $Ag_3PO_4$ has the absorption edge at about 530 nm, which is consistent with the reported result.[44] Compared with $Bi_2WO_6$, the wavelength regions of the $Ag_3PO_4/Bi_2WO_6$ composite are extended towards the visible-light region. Moreover, the more obvious red shift phenomenon is observed with increasing the $Ag_3PO_4$ loading, which implies more visible light is absorbed by the composite, and produce more $e^-$–$h^+$ pairs, further improve the photocatalytic activity.

The band gap energies of the photocatalysts are calculated according to the following equation:

$$(\alpha h\nu) = A\ (h\nu - E_g)^{n/2} \quad (1)$$

In this equation, $A$, $\alpha$, $h$, $h\nu$, and $E_g$ are constant, absorption coefficient, Planck constant, the energy of the incident photon, and band gap, respectively. And $n$ is 1 and 4 for a direct and indirect band gap semiconductor, respectively. The value of $n$ for $Bi_2WO_6$ and $Ag_3PO_4$ is 1 (ref. 20 and 45). By calculating, the band gaps of $Bi_2WO_6$ and $Ag_3PO_4$ are 2.90 and 2.45 eV, respectively. The band edge positions of photocatalysts can be determined by the empirical equations:

$$E_{VB} = X - E^e + 0.5\ E_g \quad (2)$$

$$E_{CB} = E_{VB} - E_{g,} \quad (3)$$

where $E_{VB}$ is the valence band edge potential, $E_{CB}$ is the conduction band edge potential, $X$ is the electronegativity of the semiconductor obtained from the geometric mean of the electronegativity for the component atoms (6.21 eV for $Bi_2WO_6$ and 5.965 eV for $Ag_3PO_4$), $E^e$ is the energy of free electrons on the hydrogen scale (4.5 eV), $E_g$ is the band gap energy of the semiconductor. Thus, $E_{VB}$ and $E_{CB}$ are calculated to be 3.34 eV and 0.44 eV for $Bi_2WO_6$ and 2.69 eV and 0.24 eV for $Ag_3PO_4$, respectively.

### 3.3 Photocatalytic tests

Based on the above results, the photocatalytic activities of prepared photocatalysts were evaluated by degradation of RB under visible-light irradiation. As shown in Fig. 7a, adsorption tests display all suspensions of photocatalyst and RB reach adsorption–desorption equilibrium after 1 h stirring in dark. Meanwhile, the visible-light photocatalytic activities of samples were investigated. The results show that: (1) without the catalyst, no RB is degraded under visible-light irradiation for 180 min, implying RB is relative stability under longtime irradiation; (2) in the presence of catalysts and light, the RB-degradation efficiency is greatly improved. Compared with

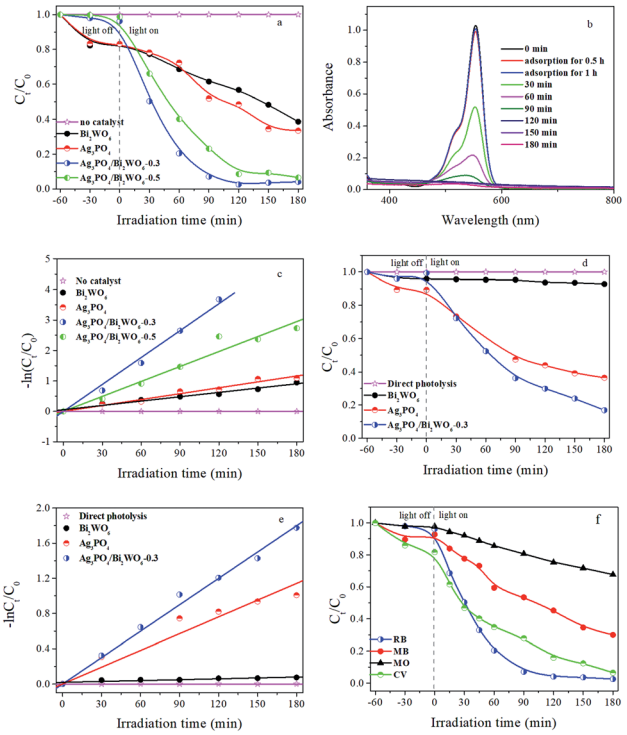


Fig. 7 Photocatalytic activities of different photocatalysts toward (a) RB, (d) Phen, and (f) different organic dyes under visible-light irradiation. (b) UV-vis absorption spectra of the RB solution separated from $Ag_3PO_4/Bi_2WO_6$-0.3 suspension under visible-light illumination. Kinetic fitting curves for photocatalytic degradation of (c) RB and (e) Phen over different photocatalysts under visible-light irradiation.

pure $Bi_2WO_6$ and $Ag_3PO_4$, $Ag_3PO_4/Bi_2WO_6$ composites show higher photocatalytic activity. Furthermore, with increasing molar ratio of $Ag_3PO_4/Bi_2WO_6$ from 0 to 0.3, $Ag_3PO_4/Bi_2WO_6$ composites display enhanced photocatalytic activity and then decrease with increasing to 0.5. For example, RB-degradation efficiency of $Bi_2WO_6$, $Ag_3PO_4$, $Ag_3PO_4/Bi_2WO_6$-0.3, and $Ag_3PO_4/Bi_2WO_6$-0.5 can reach 43.2%, 51.4%, 97.5%, and 91.4% after 120 min visible-light illumination.

Fig. 7b shows the absorption spectra of RB ($\lambda_{max} = 553$ nm) under visible-light irradiating the photoactive $Ag_3PO_4/Bi_2WO_6$-0.3. The absorption peak intensity of RB located at 553 nm reduces rapidly with prolonged irradiation time, and it is hardly observed after 120 min visible-light illumination. The results are consistent with Fig. 7a. In addition, we find the obvious blue shift of the absorption peak at 553 nm, which corresponds to the de-ethylation process. Therefore, the cleavage of the whole conjugated chromophore structure of RB leads to rapidly reducing the absorption peak intensity of RB, which indicates intermediate products were formed and then degraded to small molecules or $CO_2$ during the RB degradation process.[15,46]

The pseudo-first-order model based on the Langmuir–Hinshelwood (LH) kinetic model is mainly used to estimate the kinetics of the photocatalytic degradation of RB, as shown in the following equation:

$$-\ln(C_t/C_0) = k_{app}t, \quad (4)$$

where $k$ is the apparent rate constant of degradation; $C_t$ and $C_0$ are the initial and instantaneous concentration of RB at the time $t_0$ and $t$, respectively. Plots of $-\ln(C_t/C_0)$ *vs.* time for photocatalysts are shown in Fig. 7c. All these photocatalysts display good linear relation meeting a pseudo-first-order reaction, and the kinetic constants calculated are 0 $min^{-1}$ (no photocatalyst), 0.00515 $min^{-1}$ ($Bi_2WO_6$), 0.00646 $min^{-1}$ ($Ag_3PO_4$), 0.0295 $min^{-1}$ ($Ag_3PO_4/Bi_2WO_6$-0.3), and 0.0164 $min^{-1}$ ($Ag_3PO_4/Bi_2WO_6$-0.5), respectively. During all photocatalysts, $Ag_3PO_4/Bi_2WO_6$-0.3 shows the highest photocatalytic activity and decomposition rate, which are 5.7 and 4.6 times than that of $Bi_2WO_6$ and $Ag_3PO_4$, respectively. In short, $Ag_3PO_4/Bi_2WO_6$-0.3 exhibits the dramatical enhancement on photocatalytic activity of identical conditions than pure $Bi_2WO_6$ and $Ag_3PO_4$.

In order to eliminate the influence of dye sensitization, Phen as the colorless compound is selected as a model molecule to further study the photocatalytic performance of $Ag_3PO_4/Bi_2WO_6$ under visible-light irradiation. Because that Phen ($\lambda_{max} = 270$ nm) has no absorption and no photosensitization in visible-light region. Fig. 7d and e show the relative concentration ($C_t/C_0$) and $-\ln(C_t/C_0)$ *vs.* time curves of Phen in the presence of $Bi_2WO_6$, $Ag_3PO_4$, and $Ag_3PO_4/Bi_2WO_6$-0.3. As displayed in Fig. 7d, the direct photolysis of Phen is neglected during the whole visible-light irradiation, indicating Phen is also a stable pollutant. However, the degradation efficiency of Phen is about 7.1%, 63.5%, and 83.1% in the presence of $Bi_2WO_6$, $Ag_3PO_4$, and $Ag_3PO_4/Bi_2WO_6$-0.3, respectively. Their corresponding rate constants are obtained from Fig. 7e to be 0.00033 $min^{-1}$, 0.00634 $min^{-1}$, and 0.00999 $min^{-1}$, respectively. The results are consistent with those obtained for RB degradation. Meanwhile, the above results confirm that photocatalytic performance of $Ag_3PO_4/Bi_2WO_6$-0.3 is due to the excitation of the photocatalyst rather than the sensitization mechanism.

In order to test the extensive adaptability of the $Ag_3PO_4/Bi_2WO_6$ photocatalyst, anionic dye (MO) and cationic dyes (RB, MB, and CV) are also employed as target pollutants. As depicted in Fig. 7f, MO, RB, MB, and CV are effectively eliminated after visible-light irradiation, which implies that the $Ag_3PO_4/Bi_2WO_6$ photocatalyst is highly efficient in the visible-light degradation of pollutants, especially cationic dyes. The excellent photocatalytic activity of $Ag_3PO_4/Bi_2WO_6$ towards to organic pollutants is due to the good formation of heterostructures, which not only broaden the spectral response range to visible light but also effectively promote the charge separation. In addition, the excessive $Ag_3PO_4$ may act as a recombination center, and cover the active sites on the $Bi_2WO_6$ surface, leading to reducing the separation efficiency of the photogenerated charge carriers. It can be confirmed from the following PL results (Fig. S4, ESI†). That is why $Ag_3PO_4/Bi_2WO_6$-0.3 shows higher photocatalytic activity than $Ag_3PO_4/Bi_2WO_6$-0.5.

The photostability of a photocatalyst is essential for practical application. To research the reusability of photocatalysts, recycled photocatalytic degradation RB test was performed over $Ag_3PO_4/Bi_2WO_6$-0.3 composite. As shown in Fig. 8a, the photodegradation percentage of RB after visible light irradiation for 90 min reduced from the original 92.9–86.5%, 75.8%, 71.5%, 68.5% and 68.1% after six cycles. Although the degradation

 

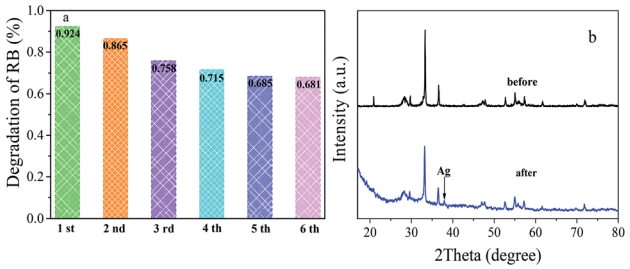


Fig. 8 Cyclic photocatalytic degradation of RB over $Ag_3PO_4/Bi_2WO_6$-0.3 (a); XRD patterns of $Ag_3PO_4/Bi_2WO_6$-0.3 before and after the cycle degradation experiments (b).

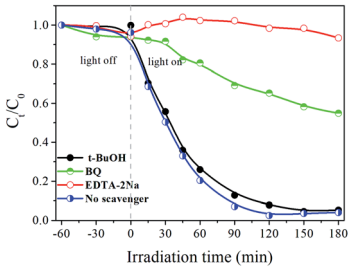


Fig. 9 Effects of different scavengers on the photodegradation of RB over the $Ag_3PO_4/Bi_2WO_6$-0.3 composite.

efficiency of RB in the reactive system went on 24.8%, the photodegradation percentage of RB was almost the same after the five and six cycles, indicating that the catalyst had a certain stability. The slight decline of photocatalytic efficiency is attributed to the inevitable loss of photocatalysts during the recycle runs. In addition, the color of RB-photocatalysts suspension had been changed from pink to black, indicating metallic Ag was formed on the surface of the catalyst during the photocatalytic process. This phenomenon is confirmed by the comparative XRD patterns of $Ag_3PO_4/Bi_2WO_6$ before and after the photocatalytic experiments in Fig. 8b. There is one weak peak located at 38.1° for $Ag_3PO_4/Bi_2WO_6$-0.3 after cycles, which can be classified as the characteristic peak of metallic silver.[47] This part Ag formed at the early photocatalytic reaction. Meanwhile, UV-vis/DRS, the high-resolution XPS spectra of Ag 3d, and SEM image of $Ag_3PO_4/Bi_2WO_6$-0.3 after reaction are also shown in Fig. S3 (ESI†). As displayed in Fig. S3(a),† $Ag_3PO_4/Bi_2WO_6$-0.3 displays enhanced photo-absorption in the visible-light region after the cycle degradation experiments. In particular, a broad prominent absorption in the visible-light region of 450–800 nm is observed, owing to the surface plasmon resonance (SPR) effect of Ag nanoparticles.[47] Fig. S3(b)† shows the Ag XPS spectra of $Ag_3PO_4/Bi_2WO_6$-0.3 after cycles. The peaks located at 368.8 and 374.9 eV are assigned to $Ag^0$, and the typical peaks located at 367.8 and 373.8 eV are ascribed to $Ag^+$. According to the XPS results, the content of $Ag^0$ is about 30% after cycles. As shown in Fig. S3(c),† although the aggregation phenomenon becomes more obvious after the photocatalytic reaction, $Ag_3PO_4/Bi_2WO_6$-0.3 still maintain their morphologies. These results further prove that the photocorrosion resistance and stability of $Ag_3PO_4$ were improved by introducing $Bi_2WO_6$ to construct $Ag_3PO_4$-Ag-$Bi_2WO_6$ Z-scheme heterostructures.

### 3.4 Photocatalytic mechanism discussion

**3.4.1 Free radical and hole scavenging experiments.** According to the photocatalytic literature,[48,49] the movement of the charge carriers such as $e^-$ and $h^+$ is the crucial parameter to generate reactive species such as $^{\cdot}O^{2-}$, $^{\cdot}OH$, and $h^+$. Thus, active species generated during the photodegradation process of RB over the $Ag_3PO_4/Bi_2WO_6$-0.3 are identified by free radical and hole trapping experiments in the presence of various scavengers such as *tert*-butyl alcohol (*t*-BuOH, $^{\cdot}OH$ scavenger, 1 mM), ethylenediaminetetraacetic acid disodium salt (EDTA-2Na, $h^+$ scavenger, 1 mM), and benzoquinone(BQ, $^{\cdot}O^{2-}$ scavenger, 1 mM).

Fig. 9 depicts the effects of various scavengers on the degradation of RB. The addition of *t*-BuOH can hardly inhibit RB degradation, which demonstrates that hydroxyl radicals $^{\cdot}OH$ have little influence in the photocatalytic process. However, when the EDTA-2Na and BQ were added into the reaction system, the photocatalytic activities of $Ag_3PO_4/Bi_2WO_6$-0.3 are obviously decelerated. Furthermore, the photodegradation percentage of RB is reduced from the original 100–6.6% and 45.1%, respectively. The above results suggested that $h^+$ and $^{\cdot}O^{2-}$ are main active species during the degradation process.

**3.4.2 Photoelectrochemical experiments.** Photoelectrochemical experiments as a useful technique to monitor the generation of photoelectrons and holes as well as their transfer and efficient separation in the $Ag_3PO_4/Bi_2WO_6$ system were performed. As shown in Fig. 10, the transient photocurrent responses of $Bi_2WO_6$, $Ag_3PO_4$, and $Ag_3PO_4/Bi_2WO_6$-0.3 are recorded for several on–off cycles under visible-light irradiation at a bias of 1 V. It is found that the photocurrent responses of the tested sample working electrodes decrease to zero as soon as the lamp is turned off, and a rapid increase appears when the light is on. Meanwhile, photocurrent responses regain a reproducible value when the lamp is turned on again during on–off intermittent irradiation cycles. In addition, the $Ag_3PO_4/Bi_2WO_6$-0.3 exhibits the enhanced the photocurrent compared with $Bi_2WO_6$ and $Ag_3PO_4$. The sequence of the photocurrent is in accordance with the order of the photocatalytic activity of photocatalysts. This suggests a smaller recombination and a more efficient separation of photo-generated $e^-$–$h^+$ pairs occurs across the interface between $Bi_2WO_6$ and $Ag_3PO_4$ in the $Ag_3PO_4/Bi_2WO_6$ composite.

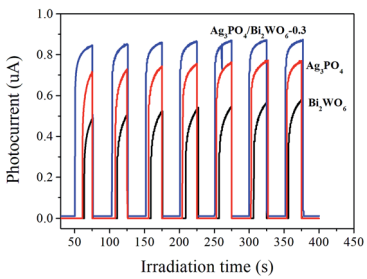


Fig. 10 Photocurrent responses of $Ag_3PO_4$, $Bi_2WO_6$, and $Ag_3PO_4/Bi_2WO_6$-0.3 under visible light irradiation.

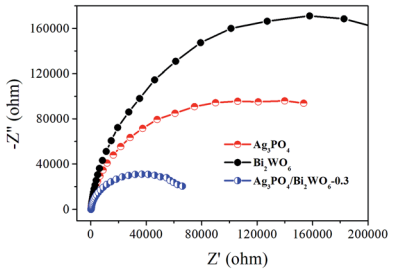


Fig. 11 EIS Nyquist plots of $Ag_3PO_4$, $Bi_2WO_6$, and $Ag_3PO_4/Bi_2WO_6$-0.3.

Electrochemical impedance spectroscopy (EIS) is also employed to investigate the charge transfer resistance and the separation of photogenerated $e^-$–$h^+$ pairs at solid/electrolyte interfaces in the photocatalyst.[50] Fig. 11 displays the EIS Nyquist plots of $Bi_2WO_6$, $Ag_3PO_4$, and $Ag_3PO_4/Bi_2WO_6$-0.3 under visible-light irradiation. It is clearly seen that the smallest arc radius of the EIS Nyquist plot of $Ag_3PO_4/Bi_2WO_6$-0.3 implies that it has the fastest interfacial electron transfer and more separation of photogenerated $e^-$–$h^+$ pairs when compared to those of $Bi_2WO_6$ and $Ag_3PO_4$. It is the reason for the $Ag_3PO_4/Bi_2WO_6$-0.3 composites exhibit the highest photocatalytic activity.

Photoluminescence (PL) spectrum is also an effective tool to reveal the migration, transfer and recombination processes of the photogenerated $e^-$–$h^+$ pairs in semiconductors. Usually, a lower PL intensity indicates lower recombination rate of the charge carriers and higher photocatalytic activities of the photocatalysts. Fig. S4 (ESI†) shows the PL spectra of as-prepared $Ag_3PO_4$, $Bi_2WO_6$, and $Ag_3PO_4/Bi_2WO_6$ composites with an excitation wavelength of 360 nm. As for the $Bi_2WO_6$-based materials, their PL intensities follow the order $Bi_2WO_6$ > $Ag_3PO_4/Bi_2WO_6$-0.5 > $Ag_3PO_4/Bi_2WO_6$-0.3 > $Ag_3PO_4$. Compared with pure $Bi_2WO_6$, the PL intensities of $Ag_3PO_4/Bi_2WO_6$ composites present an obvious decrease, implying a lower recombination feasibility of free charges in the $Ag_3PO_4/Bi_2WO_6$ heterostructures. The $Ag_3PO_4/Bi_2WO_6$ nanocomposite displays a higher PL intensity than $Ag_3PO_4$, implying that the migration pathways of the photoexcited $e^-$–$h^+$ in the $Ag_3PO_4/Bi_2WO_6$ nanocomposite is plasmonic Z-scheme theory (Scheme 1a) not as heterojunction energy-band theory (Scheme 1b).[51,52]

From the Scheme 1a, under visible-light irradiation, both $Bi_2WO_6$ and $Ag_3PO_4$ can be excited to produce $e^-$ and $h^+$ simultaneously owing to their visible-light response. On the one hand, the part of $Ag_3PO_4$ can be photoreduced to $Ag^0$ during the initial photocatalytic process. Ag nanoparticles (NPs) can absorb visible light and induce $e^-$–$h^+$ pairs on account of the dipolar character and the SPR effect of the Ag NPs. The photogenerated electrons in the CB of $Ag_3PO_4$ shift to the photogenerated holes produced by plasmonic absorption in the Ag NPs, which results in higher PL intensity. On other the hand, the plasmon hot electrons generated by the localized SPR oscillations of Ag NPs can capture the dissolved $O_2$ in water to form $^{\cdot}O^{2-}$ (ref. 53). Meanwhile, the plasmon hot electrons directly transfer from the Ag NPs to the CB of $Bi_2WO_6$. While the photogenerated holes are still in the VB of $Ag_3PO_4$ and $Bi_2WO_6$.

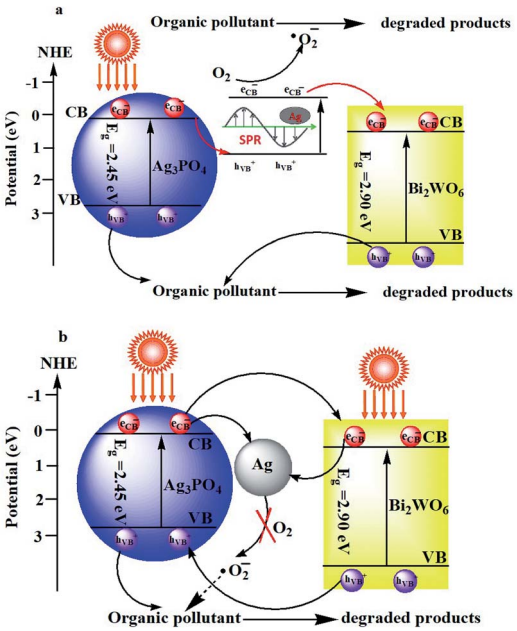


Scheme 1 schematic diagram of the separation and transfer of photogenerated charges in the $Ag_3PO_4/Bi_2WO_6$ heterostructures based on the plasmonic Z-scheme theory (a) and heterojunction energy-band theory (b) under visible light irradiation.

Therefore, the photo-generated charge carriers are efficiently separated in space, which retards the photocorrosion of $Ag_3PO_4$. With the assistance of $h^+$ and $^{\cdot}O^{2-}$ the two main active species, the organic pollutant is effectively degraded in aqueous solution. But from the heterojunction energy-band theory described in Scheme 1b, the VB potential (2.68 eV *vs.* NHE) of $Ag_3PO_4$ is more negative than that of $Bi_2WO_6$ (3.08 eV *vs.* NHE), which leads to the migration of the $h^+$ from $Bi_2WO_6$ to $Ag_3PO_4$. Since the CB potential (0.24 eV *vs.* NHE) of $Ag_3PO_4$ is more negative than that of $Bi_2WO_6$ (0.44 eV *vs.* NHE), photo-induced electrons from $Ag_3PO_4$ migrate to the CB of $Bi_2WO_6$ and then transfer to $Ag^0$. Therefore, the photo-generated electrons cannot reduce $O_2$ to produce $^{\cdot}O^{2-}$, due to the CB potential of $Bi_2WO_6$ being more positive than the redox potential of $^{\cdot}O^{2-}$ formation ($O_2/^{\cdot}O^{2-}$ = −0.33 eV, NHE).[51] Thus this phenomenon cannot explain the stronger effect of $^{\cdot}O^{2-}$ on the degradation of RB. In conclusion, the plasmonic Z-scheme theory for the photocatalysis of $Ag_3PO_4/Bi_2WO_6$ is much more reasonable.

## 4. Conclusions

Novel $Ag_3PO_4/Bi_2WO_6$ heterostructured materials were successfully synthesized by assembling $Ag_3PO_4$ irregular nanospheres on the surface of $Bi_2WO_6$ nanoflakes. $Ag_3PO_4/Bi_2WO_6$-0.3 showed obviously superior visible-light catalytic activity toward degradation of organic pollutants. Free radical and hole scavenging experiments suggested $h^+$ and $^{\cdot}O^{2-}$ are two main active species through the degradation process. In brief, the enhanced photocatalytic activity was due to the good formation of heterostructures, which could not only broaden the spectral response range to visible light but also effectively promoted the charge separation. These results were solidly confirmed by

photocurrent responses, electrochemical impedance spectroscopy, and photoluminescence spectrum. In addition, $Ag_3PO_4$/$Bi_2WO_6$-0.3 exhibited relative higher photostability toward RB degradation, which was explained by the reasonable photoreactive mechanism. This work provides the potential application of $Bi_2WO_6$-based heterostructures as efficient visible light responsive catalysts for environmental remediation.

## Conflicts of interest

There are no conflicts to declare.

## Acknowledgements

This work is supported by The Fundamental Research Funds in Heilongjiang Provincial Universities (135109204).

## Notes and references

1 Q. J. Xiang, D. Lang, T. T. Shen and F. Liu, *Appl. Catal., B*, 2015, **162**, 196.
2 J. H. Kou, C. H. Lu, J. Wang, Y. K. Chen, Z. Z. Xu and R. S. Varma, *Chem. Rev.*, 2017, **117**, 1445.
3 K. Wenderich and G. Mul, *Chem. Rev.*, 2016, **116**, 14587.
4 H. Huang, N. Huang, Z. H. Wang, G. Q. Xia, M. Chen, L. L. He, Z. F. Tong and C. G. Ren, *J. Colloid Interface Sci.*, 2017, **502**, 77.
5 H. Wei, W. A. McMaster, J. Z. Y. Tan, L. Cao, D. H. Chen and R. A. Caruso, *J. Phys. Chem. C*, 2017, **121**, 22114.
6 P. Mazierski, J. Nadolna, G. Nowaczyk, W. Lisowski, M. J. Winiarski, T. Klimczuk, M. P. Kobylański, S. Jurga and A. Zaleska-Medynska, *J. Phys. Chem. C*, 2017, **121**, 17215.
7 R. F. Tang, H. F. Su, Y. W. Sun, X. X. Zhang, L. Li, C. H. Liu, S. Y. Zeng and D. Z. Sun, *J. Colloid Interface Sci.*, 2016, **466**, 388.
8 F. Chen, Q. Yang, J. Sun, F. B. Yao, S. N. Wang, Y. L. Wang, X. L. Wang, X. M. Li, C. G. Niu, D. B. Wang and G. M. Zeng, *ACS Appl. Mater. Interfaces*, 2016, **8**, 32887.
9 Z. Dai, F. Qin, H. P. Zhao, J. Ding, Y. L. Liu and R. Chen, *ACS Catal.*, 2016, **6**, 3180.
10 J. Li, Y. C. Yin, E. Z. Liu, Y. N. Ma, J. Wan, J. Fan and X. Y. Hu, *J. Hazard. Mater.*, 2017, **321**, 183.
11 J. Song, L. Zhang, J. Yang, X. H. Huang and J. S. Hu, *Ceram. Int.*, 2017, **43**, 9214.
12 J. Song, L. Zhang, J. Yang, X. H. Huang and J. S. Hu, *Mater. Des.*, 2017, **123**, 128.
13 L. Zhang, X. F. Cao, X. T. Chen and Z. L. Xue, *J. Colloid Interface Sci.*, 2011, **354**, 630.
14 X. B. Zhang, L. Zhang, J. S. Hua and X. H. Huang, *RSC Adv.*, 2016, **6**, 32349.
15 Y. K. Huang, S. F. Kang, Y. Yang, H. F. Qin, Z. J. Ni, S. J. Yang and X. Li, *Appl. Catal., B*, 2016, **196**, 89.
16 C. M. Zhang, G. Chen, C. M. Li, J. X. Sun, C. Lv, S. Fan and W. N. Xing, *ACS Sustainable Chem. Eng.*, 2016, **4**, 5936.
17 X. J. Chen, Y. Z. Dai and X. Y. Wang, *J. Alloys Compd.*, 2015, **649**, 910.
18 X. F. Yang, J. L. Qin, Y. Jiang, R. Li, Y. Li and H. Tang, *RSC Adv.*, 2014, **4**, 18627.
19 Y. P. Bi, S. X. Ouyang, N. Umezawa, J. Y. Cao and J. H. Ye, *J. Am. Chem. Soc.*, 2011, **133**, 6490.
20 Z. G. Yi, J. H. Ye, N. Kikugawa, T. Kako, S. X. Ouyang, H. Stuart-Williams, H. Yang, J. Y. Cao, W. J. Luo, Z. S. Li, Y. Liu and R. L. Withers, *Nat. Mater.*, 2010, **9**, 559.
21 X. F. Yang, H. Tang, J. S. Xu, M. Antonietti and M. Shalom, *ChemSusChem*, 2015, **8**, 1350.
22 X. F. Yang, Z. P. Chen, J. S. Xu, H. Tang, K. M. Chen and Y. Jiang, *ACS Appl. Mater. Interfaces*, 2015, **7**, 15285.
23 X. Y. Zhang, H. X. Zhang, Y. Y. Xiang, S. B. Hao, Y. X. Zhang, R. N. Guo, X. W. Cheng, M. Z. Xie, Q. F. Cheng and B. Li, *J. Hazard. Mater.*, 2018, **342**, 353.
24 L. Zhou, O. G. Alvarez, C. S. Mazon, L. Chen, H. P. Deng and M. H. Sui, *Catal. Sci. Technol.*, 2016, **6**, 5972.
25 J. Tian, T. J. Yan, Z. Qiao, L. L. Wang, W. J. Li, J. M. You and B. B. Huang, *Appl. Catal., B*, 2017, **209**, 566.
26 Q. S. Li and C. Yang, *Mater. Lett.*, 2017, **199**, 168.
27 L. J. Xu, Y. D. Wang, J. Liu, S. G. Han, Z. P. Pan and L. Gan, *J. Photochem. Photobiol., A*, 2017, **340**, 70.
28 X. Lin, X. Y. Guo, W. L. Shi, F. Guo, G. B. Che, H. J. Zhai, Y. S. Yan and Q. W. Wang, *Catal. Commun.*, 2015, **71**, 21.
29 X. Lin, J. Hou, S. S. Jiang, Z. Lin, M. Wang and G. B. Che, *RSC Adv.*, 2015, **5**, 104815.
30 W. L. Shi, F. Guo and S. L. Yuan, *Appl. Catal., B*, 2017, **209**, 720.
31 Q. Y. Li, F. L. Wang, Y. X. Hua, Y. T. Luo, X. H. Liu, G. R. Duan and X. J. Yang, *J. Colloid Interface Sci.*, 2017, **506**, 207.
32 S. Jonjana, A. Phuruangrat, T. Thongtem, B. Kuntalue and S. Thongtem, *Mater. Lett.*, 2018, **218**, 146.
33 X. Cui, Y. F. Zheng, H. Zhou, H. Y. Yin and X. C. Song, *J. Taiwan Inst. Chem. Eng.*, 2016, **60**, 328.
34 L. Wang, Y. Y. Chai, J. Ren, J. Ding, Q. Q. Liu and W. L. Dai, *Dalton Trans.*, 2015, **44**, 14625.
35 X. F. Qian, D. T. Yue, Z. Y. Tian, M. Reng, Y. Zhu, M. Kan, T. Y. Zhang and Y. X. Zhao, *Appl. Catal., B*, 2016, **193**, 16.
36 Y. N. Guo, L. Chen, X. Yang, F. Y. Ma, S. Q. Zhang, Y. X. Yang, Y. H. Guo and X. Yuan, *RSC Adv.*, 2012, **2**, 4656.
37 N. Wei, H. Z. Cui, M. L. Wang, X. Z. Wang, X. J. Song, L. Ding and J. Tian, *RSC Adv.*, 2017, **7**, 18392.
38 S. Z. You, Y. Hu, X. C. Liu and C. H. Wei, *Appl. Catal., B*, 2018, **232**, 288.
39 J. Wan, X. Du, E. Z. Liu, Y. Hu, J. Fan and X. Y. Hu, *J. Catal.*, 2017, **345**, 281.
40 J. X. Xia, J. Dai, S. Yin, H. Xu, J. Zhang, Y. G. Xu, L. Xu, H. M. Li and M. X. Ji, *RSC Adv.*, 2014, **4**, 82.
41 J. Di, J. X. Xia, Y. P. Ge, H. P. Li, H. Y. Ji, H. Xu, Q. Zhang, H. M. Li and M. N. Li, *Appl. Catal., B*, 2015, **168–169**, 51.
42 N. N. Wang, Y. Zhou, C. H. Chen, L. Y. Cheng and H. M. Ding, *Catal. Commun.*, 2016, **73**, 74.
43 R. F. Tang, H. F. Su, S. X. Duan, Y. W. Sun, L. Li, X. X. Zhang, S. Y. Zeng and D. Z. Sun, *RSC Adv.*, 2015, **5**, 41949.
44 X. Lin, J. Hou, S. S. Jiang, Z. Lin, M. Wang and G. B. Che, *RSC Adv.*, 2015, **5**, 104815.
45 W. K. Jo, J. Y. Lee and T. S. Natarajan, *Phys. Chem. Chem. Phys.*, 2016, **18**, 1000.

46 X. Lin, X. Y. Guo, W. L. Shi, F. Guo, G. B. Che, H. J. Zhai, Y. S. Yan and Q. W. Wang, *Catal. Commun.*, 2015, **71**, 21.
47 T. Cai, Y. T. Liu, L. L. Wang, S. Q. Zhang, Y. X. Zeng, J. L. Yuan, J. H. Ma, W. Y. Dong, C. B. Liu and S. L. Luo, *Appl. Catal., B*, 2017, **208**, 1.
48 A. Kaur and S. K. Kansal, *Chem. Eng. J.*, 2016, **302**, 194.
49 B. Panigrahy and S. Srivastava, *New J. Chem.*, 2016, **40**, 3370.
50 L. Liu, Y. H. Qi, J. R. Lu, S. L. Lin, W. J. An, Y. H. Liang and W. Q. Cui, *Appl. Catal., B*, 2016, **183**, 133.
51 S. P. Wan, M. Ou, Q. Zhong and S. L. Zhang, *New J. Chem.*, 2018, **42**, 318.
52 S. F. Chen, L. Ji, W. M. Tang and X. L. Fu, *Dalton Trans.*, 2013, **42**, 10759.
53 H. Tang, Y. H. Fu, S. F. Chang, S. Y. Xie and G. G. Tang, *Chin. J. Catal.*, 2017, **38**, 337.